

Role of ocean dynamics on mesoscale and sub-mesoscale variability of Ekman pumping for the Bay of Bengal using SCATSAT-1 forced ocean model simulations

Smitha Ratheesh*, Aditya Chaudhary, Neeraj Agarwal and Rashmi Sharma

Oceanic Sciences Division, Space Applications Centre, ISRO, Ahmedabad 380 015, India

Role of ocean dynamics on vertical velocity of Ekman pumping (VVE) is analysed using simulations from very high resolution Ocean General Circulation Model (OGCM) configured for the Bay of Bengal (BoB). For this purpose, OGCM is forced with SCATSAT-1 scatterometer wind fields for 2017. Three mechanisms which modify VVE in the ocean are addressed in this study; the first results from the influence of sea surface temperature (SST) on wind field, and the other two arise from the influence of ocean surface currents (OSCs) on the wind field. Analysis for different length scales ranging from mesoscale to sub-mesoscale is also carried out. The results suggest a significant role of ocean dynamics on VVE, especially over sub-mesoscale range (spatial scales of the order of 2–10 km). Relative vorticity of OSC-induced Ekman pumping is found to be quite high (~3 m/day) at 2 km length scale, especially along the periphery of mesoscale eddies and along the filament structures. Impact of SST on VVE is least amongst the three factors and is observed to be significant only up to the length scales of 30 km. For length scales less than 10 km, relative vorticity-induced Ekman pumping increases drastically and the total Ekman pumping vertical velocity is predominantly controlled by the relative vorticity of OSC-induced Ekman pumping only.

Keywords: Ekman pumping, ocean dynamics, scatterometers, vertical velocity, wind field.

Introduction

ACCURATE estimation of vertical velocity of Ekman pumping (VVE) is a major oceanographic challenge as the VVE-induced exchange of tracers varies across different length scales from mesoscale to sub-mesoscale¹. Except for mixing due to winter convection, wind-driven mixing is the dominant mechanism that determines exchange between surface and subsurface waters. Vertical velocity associated with Ekman pumping significantly

affects the vertical transfer of tracers within or below mixed layer of ocean through vertical mixing. Proper estimation or simulation of VVE plays a significant role in closing many of the tracer budgets, including those of nutrients across wide regions of the ocean². VVE depends on the extent of Ekman depth, up to which the explicit role of wind on ocean is significant. It determines the strength of wind-driven upwelling/downwelling³, and regulates the blooming of phytoplankton on surface waters. Positive VVE (upwelling) helps replenish the surface waters with the subsurface nutrients and plays an important role in fishery⁴. However, ocean dynamics plays an important role in modifying the low-level wind field⁵ and hence the vertical velocity induced by Ekman pumping. Modification of the mechanical input to the ocean waters due to ocean dynamics is a subject of active research in oceanography and requires a detailed study. Large-scale air–sea interaction mechanisms in the Bay of Bengal (BoB) have been studied using spaceborne measurements⁶. However, there is not much detailed information on the role of ocean dynamics on VVE at a finer scale (sub-mesoscale) in the BoB due to lack of observations. A study done using a high-resolution coupled atmosphere–ocean–wave shed some light on the sub-mesoscale characteristics and their interaction with fronts in the BoB⁷. Dynamics of the sub-mesoscale features in the BoB and its influence on air–sea interaction is being actively studied under Air–Sea Interactions in the Northern Indian Ocean (ASIRI)–Ocean Mixing and Monsoons (OMM) programme⁸.

The coupled interaction between ocean and atmosphere at the sea surface plays a critical role in modifying the marine atmospheric boundary layer (MABL)⁵. Wind blowing over the sea surface imparts momentum to the ocean, which forces upper ocean currents and generates evaporative cooling at the sea surface. These turbulent fluxes in turn affect the circulation in MABL. This coupled interaction at the ocean surface varies critically at different length scales in the ocean⁹ and for various components of ocean dynamics¹⁰ such as sea surface temperature (SST) and ocean currents. Oceanic circulation is characterized not only by large-scale currents, but

*For correspondence. (e-mail: smitha@sac.isro.gov.in)

also by energetic mesoscale structures (ranging from ~10–200 km in space)¹¹ and additionally, by sub-mesoscale structures (<10 km)^{12,13}.

Sub-mesoscale and mesoscale processes modify the vertical exchange of tracers such as temperature, salinity, nutrients, etc. from surface to deeper ocean and vice versa¹, mainly due to air–sea interaction-induced altered mixing rates^{10,14}. This includes the effect of ocean surface currents (OSCs) on the relative wind field and hence on the surface stress¹⁰. In addition, the spatial variations of SST generate local changes in the advective accelerations of near-surface atmosphere flow by modulating the drag and pressure variations within the MABL⁹. However, this coupling between SST and wind varies spatially and seasonally, and is fundamentally different for oceanic mesoscale ranges^{5,15,16}. Air–sea interactions at mesoscale and sub-mesoscale exhibit positive correlation between SST and wind speed^{17,18}, revealing the role of ocean as a driving engine for the atmosphere. This is in contrast to the negative correlation between these variables over large climate scales¹⁹, indicating that the atmosphere drives the ocean.

Satellite scatterometer has proved its efficiency in providing spatially extensive wind measurements with higher accuracy than the any available numerical weather prediction (NWP) models^{20,21}. Temporal and spatial coverage from scatterometer are capable of retrieving small-scale features in the wind field⁵. To continue the heritage of scatterometer, Indian Space Research Organisation (ISRO) launched SCATSAT-1 in October 2016. This is ISRO's second spaceborne scatterometer to measure the near-surface wind vectors at Ku-band over the ocean at a global scale, to provide continuity of ocean surface wind vector observations for various applications such as weather prediction, ocean state prediction, etc.

Simulations from very high resolution ocean models have revealed their importance in studying sub-mesoscale features, ranging from 1 to 10 km in the spatial scale²² and are inevitable to study sub-mesoscale processes in the current scenario of ocean observations from space and *in situ*, which have their own limitations. Scatterometer wind forced simulations are more close to reality compared to the reanalysis wind fields forced model simulations²⁰. Hence in the present study, a very high-resolution (2 km) Ocean General Circulation Model (OGCM) is configured for the BoB and outputs from the OGCM forced with SCATSAT-1 wind data are utilized to understand the role of ocean dynamics in regulating air–sea interaction. The analysis is carried out by quantifying the relative contribution of SST and OSC in VVE for the BoB. The primary objective of the study is to assess and quantify the various contributions to VVE that arise from the effect of relative motion between ocean and air, relative vorticity of OSC and effect of SST on wind stress over different length scales ranging from 2 to 100 km.

Data and methodology

To conduct the experiments, model simulations from a very high-resolution OGCM are used. The ocean model used is the Massachusetts Institute of Technology General Circulation Model (MITGCM)²³. For the present study, MITGCM is configured specifically for the BoB at a 2 km × 2 km horizontal resolution with 66 levels in the vertical. The model domain is from 79°E to 100°E and from 9°N to 23°N. Bathymetry used in the model is originally from the US National Geophysical Data Centre that was modified for the Indian region²⁴. Initial conditions of temperature, salinity and velocity for 2013 are used to initialize the model. These are taken from a 10 km × 10 km Indian Ocean model²⁵, and remapped onto the high-resolution model grid using Gaussian interpolation. The model was integrated forward in time using the six-hourly European Centre for Medium-Range Weather Forecasts (ECMWF) reanalysis (ERA-Interim) dataset of winds, specific humidity, air temperature, precipitation and radiation²⁶. The southern boundary is relaxed to six-hourly fields of temperature, salinity and velocity from the 10 km × 10 km Indian Ocean model simulations available from Mallick *et al.*²⁵. Monthly climatology of Ganges–Brahmaputra river discharge values prepared from satellite altimeter-derived run-off²⁷, and Godavari and Irrawaddy discharge values²⁸ were used to compute river discharge in the model. The model integration period using ERA-Interim fluxes was from 2013 to 2016. Using initial conditions of temperature, salinity and velocity from this run, the model is further integrated using SCATSAT-1 winds for 2017. These winds are available at 25 km horizontal resolution on a daily basis from <http://mosdac.gov.in>, and have been validated recently²⁹. The efficiency of SCATSAT-1 winds in simulating ocean features is analysed using an inter-comparison model run performed with National Centre for Medium Range Weather Forecasting (NCMRWF, <ftp://ftp.ncmrwf.gov.in>) wind and flux forced model simulations, and SCATSAT-1 wind forced model simulations. For this, daily averaged NCMRWF datasets of specific humidity, air temperature, precipitation and radiation were also used to force the model for 2017. Wave spectra of sea level anomaly (SLA) from both simulations are compared with that of altimeter Jason 3. This altimeter is at an elliptical orbit with an inclination of 66.05°, a perigee of 1331.7 km and an apogee of 1343.7 km at an altitude of 1336 km. The repeat cycle of Jason-3 is 10 days and covers 95% of ice-free ocean. Jason-3 is a dual frequency altimeter, operating in the Ku (13.6 GHz) and C (5.3 Hz) bands. Model SST from both runs (forced with NCMRWF and SCATSAT-1 winds) are compared with high-resolution SST from L4 gridded GHRSSST, and downloaded from Global Data Archiving Centre (GDAC) of NASA JPL, USA (<http://podaac.jpl.nasa.gov/>). GHRSSST is available at 1 km resolution and was regridded to 2 km for comparison with the model.

Ocean interior is influenced by the stress from wind on the ocean surface through Ekman pumping. The Ekman pumping velocity and impact of SST and OSC on VVE are computed using the following equations^{10,30}. For brevity, we briefly describe different components affecting the Ekman pumping velocity.

The total Ekman pumping velocity is

$$w_{\text{tot}} = \frac{\nabla \times \bar{\boldsymbol{\tau}}}{\rho_0 f}, \quad (1)$$

where $\bar{\boldsymbol{\tau}}$ is the wind stress, ρ_0 the density of water and f is the coriolis parameter.

Wind stress does not depend entirely on wind speed. It actually depends on the relative motion between ocean and air flow. The surface stress can be modified by the relative field of wind $\bar{\mathbf{u}}_{\text{rel}}$ and can be expressed as

$$\bar{\mathbf{u}}_{\text{rel}} = \bar{\mathbf{u}}_{\text{bg}} - \bar{\mathbf{u}}_0, \quad (2)$$

where $\bar{\mathbf{u}}_{\text{bg}}$ is the smooth, large-scale background absolute wind vector and $\bar{\mathbf{u}}_0$ is the surface ocean current vector. For the present study, wind vector from SCATSAT-1 is used as the background wind field.

Mesoscale variations of SST have a significant effect on local wind stress and this SST-induced surface wind stress curl is linearly related to the local cross-wind SST gradient in SST frontal regions³¹. Hence, perturbation on surface wind stress curl through SST variability can be expressed as

$$\nabla \times \bar{\boldsymbol{\tau}}_{\text{sst}} = -\alpha \frac{\partial \mathbf{T}}{\partial n}. \quad (3)$$

The cross-wind SST gradient ($\partial \mathbf{T} / \partial n$) is calculated from the meridional ($\partial \mathbf{T} / \partial y$) and zonal ($\partial \mathbf{T} / \partial x$) SST gradient components, and α is the coupling coefficient which varies regionally and temporally, depending primarily on the magnitude of the background surface stress field. However, for the present study, we have used a global constant of 0.013 N/m²/°C for the coupling coefficient.

The total Ekman pumping can be decomposed into individual terms by separating the components of surface wind stress influenced by SST and OSC¹⁰. There are two ways that OSC modifies the wind stress field. The first contribution results from the relative motion between ocean and air, which is referred to as current-induced linear Ekman pumping (relative wind field). The second contribution arises from the relative vorticity of OSC and is not linear.

Thus, w_{tot} can be decomposed as

$$w_{\text{tot}} = w_c + w_{\text{SST}} + w_\zeta + w_{\text{noise}}, \quad (4)$$

where

$$w_c = \frac{\rho_a C_D}{\rho_0 (f + \zeta)} \nabla \times [(\bar{\mathbf{u}}_{\text{bg}} - \bar{\mathbf{u}}_0) \bar{\mathbf{u}}_{\text{bg}} - \bar{\mathbf{u}}_0], \quad (5)$$

$$w_{\text{SST}} = \frac{\nabla \times \bar{\boldsymbol{\tau}}_{\text{sst}}}{\rho_0 (f + \zeta)} = \frac{-\alpha}{\rho_0 (f + \zeta)} \frac{\partial \mathbf{T}}{\partial n}, \quad (6)$$

$$w_\zeta = \frac{1}{\rho_0 (f + \zeta)^2} \left(\boldsymbol{\tau}_x \frac{\partial \zeta}{\partial y} - \boldsymbol{\tau}_y \frac{\partial \zeta}{\partial x} \right), \quad (7)$$

where w_c is the linear Ekman pumping from the effects of surface ocean currents on stress, w_{SST} the Ekman pumping from SST influences on the surface winds, w_ζ the Ekman pumping from the effects of relative vorticity ζ of surface currents and w_{noise} is the Ekman pumping from small-scale meteorological variability, which is considered as noise in the present context.

SST and OSC simulations from the model are used along with SCATSAT-1 wind vector to compute different terms: w_{tot} , w_{SST} , w_c and w_ζ . Before using eqs (1)–(7), the fields from 2 km model run are spatially smoothed over different length scales of sub-mesoscale and meso-scale, ranging from 2 to 100 km according to the length scale to be studied. The spatial length scales chosen for the study are 2, 5, 8, 10, 15, 20, 30, 40, 50, 70 and 100 km.

The strength of the temporal variability of VVE is studied using interquartile range (IQR). The strength of the variability of any parameter can be expressed by its range, defined by the difference between maximum and minimum values of the parameter. Since range is sensitive to the extreme values of the parameter, it can mislead the interpretation of actual variability. In order to express the strength of variability IQR is used which is defined (eq. (8)) as the difference between upper ($q_{0.75}$) and lower ($q_{0.25}$) quartiles. In this way, IQR specifies the range of the central 50% of the data and is robust to the extreme value.

$$\text{IQR} = q_{0.75} - q_{0.25}. \quad (8)$$

Results and discussion

Before using SCATSAT-1 winds to study the role of ocean dynamics on VVE, it is worthwhile to analyse the efficiency of these winds over the available NWP winds. For this, a twin experiment was performed; one in which the OGCM was forced using NCMRWF winds and another with SCATSAT-1 winds, keeping all other forcing parameters the same (from NCMRWF) in both simulations. The purpose behind this was to assess the performance of the two winds in simulating meso-scale/sub-mesoscale variability in the BoB. An efficient method suggested by some researchers is to understand the spectral content in ocean variability^{32,33}. In this work, the same approach has been followed. Wavenumber spectra of SLA from Jason-3 and model simulations have been obtained over many tracks of the altimeter Jason-3.

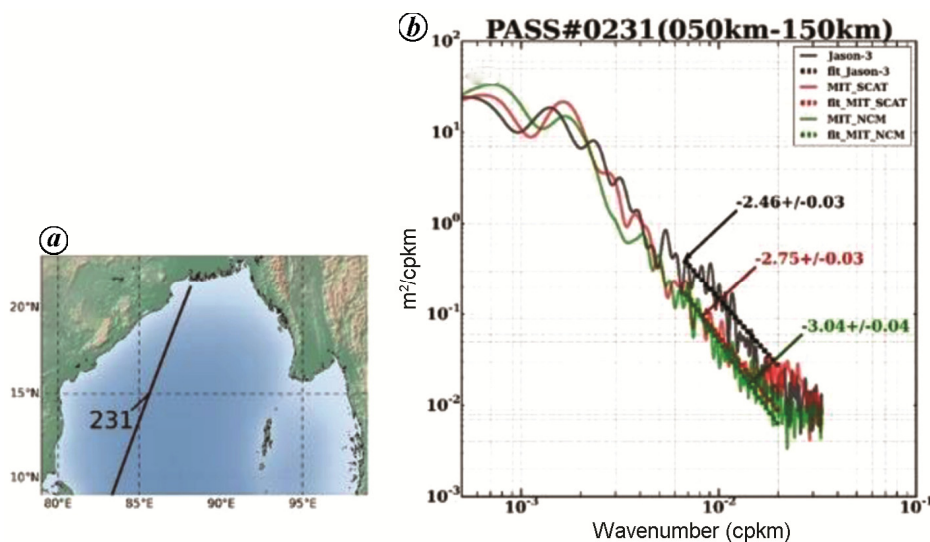


Figure 1. (a) Track 231 of Jason3 altimeter and (b) sea level anomaly wavenumber spectra of Jason-3 from model simulations (NCMRWF wind and SCATSAT-1 wind).

However, for the representation, we show results from one track numbered 231 (Figure 1 a). Power spectral density (PSD) was computed for all the cycles (33–46), covering the period January through May 2017. We are aware that this is a short length of data for computing PSD; nevertheless, one can still get an idea about the spectral content. Delayed mode data of Jason-3 were not available beyond May 2017. PSD was computed on the altimeter along-track data available at every 14 km spacing. Model SLA fields were interpolated onto Jason-3 along-track points before computing PSD. In Figure 1 b, SLA wavenumber spectra of Jason-3 and also from model simulations (NCMRWF wind and SCATSAT-1 wind) are shown. As can be seen from the figure, the model in general agrees with the altimetry in terms of shape of the spectra and also amplitude down to 50 km wavelength. One point worth noticing here is that model spectra from both the simulations are slightly underestimated in the spectral range 150 to nearly 50 km as against the altimeter. Spectral slopes computed in the wavelength range 50–150 km are also shown in the same figure. From these slopes, it can be seen that SCATSAT-1 wind forced slope is more closer to altimetry. Also, at small-scale wavelengths, SCATSAT-1 PSD agrees better with altimetry compared to NCMRWF wind forced simulations.

Model simulated SST from both the runs are compared with GHRSSST, and Figure 2 shows the root mean square error (RMSE) and correlation coefficient from both the runs. From the comparison it is clear that the model simulated SST forced with SCATSAT-1 wind shows better performance in terms of high correlation and low RMSE all over the BoB. The superiority of the SCATSAT-1 forced OGCM simulations is visible, especially along the southern part of the western and eastern boundaries of the BoB. The usefulness of scatterometer winds in accurate

simulation of ocean state has also been demonstrated in an earlier study²⁰. In the present study, simulations from model forced with SCATSAT-1 have been utilized to understand the impact of ocean dynamics on wind-induced Ekman vertical velocity.

Impact of ocean dynamics over the vertical velocity of Ekman pumping is analysed by computing VVE for different components of ocean dynamics using eqs (1)–(7). This includes the contribution from interaction of OSC and SST with ocean surface winds over sub-mesoscale and mesoscale length scales less than 100 km. Figures 3–5 show the monthly average of VVE for August 2017 induced from the influence of interaction of OSC with relative wind field, relative vorticity of OSC and SST respectively. The figures show VVE over spatial scales of 2, 8, 15, 30, 50 and 100 km. It can be seen that the fine features of Ekman pumping are more distinct at smaller length scales and are better resolved for 2 km length scale. As expected, these fine features are absent at large length scales. From Figure 3, the impact of relative wind fields on computation of Ekman velocity is evident and is found to be stronger along the western coast of the BoB. This is attributed to the strong coastal currents which significantly modulate wind stress input to the ocean along the coastal regions. Strong upwelling (positive values of VVE) can be seen along the north of 15°N along the western boundary of the BoB, where the southern part of the western BoB is more prone to downwelling (negative values of VVE). The western boundary of the BoB witnesses strong seasonally reversing coastal currents, mesoscale eddies and frontal structures compared to the rest of the BoB. During August, northward-flowing coastal currents under the influence of southwest monsoon winds promote upwelling, which brings cold subsurface water to the surface along the western boundary of the BoB. However,

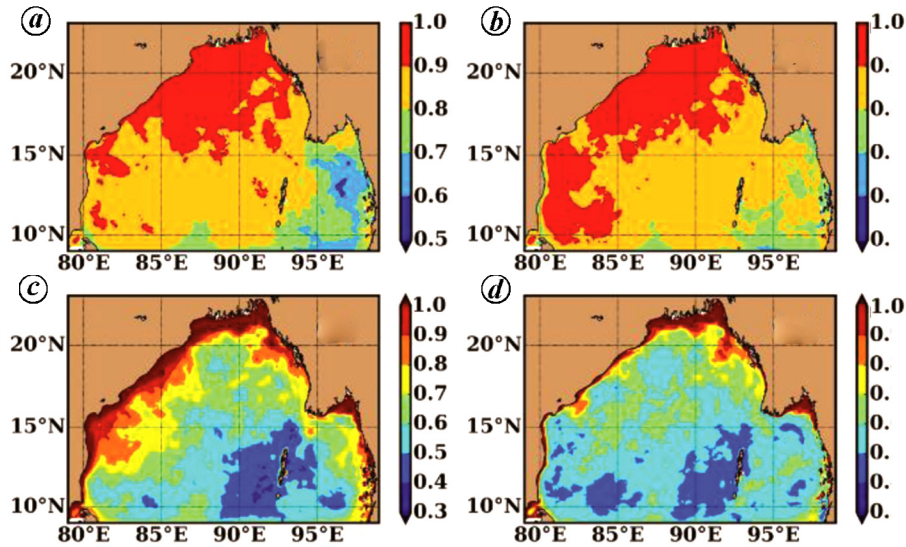


Figure 2. (Upper panel) Correlation coefficient and (lower panel) root mean square error of model sea surface temperature (SST) forced with (a and c) NCMRWF wind and (b and d) SCATSAT wind respectively computed with respect to GHRSSST for the year 2017.

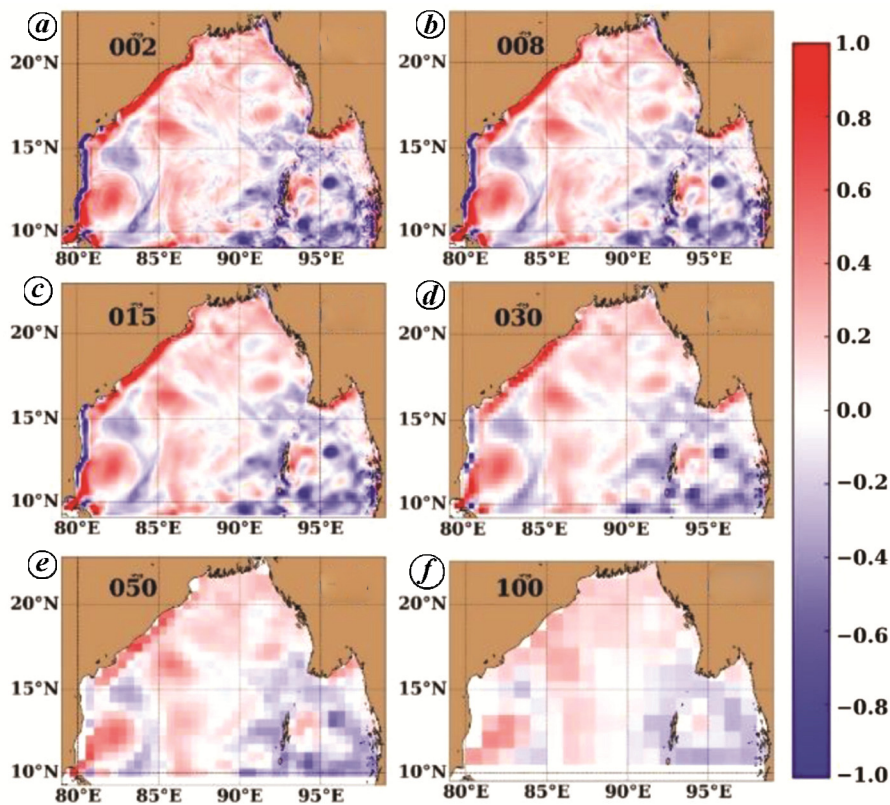


Figure 3. Monthly average of w_e (m/day) for August 2017 for different length scales: (a) 2 km, (b) 8 km, (c) 15 km, (d) 30 km, (e) 50 km and (f) 100 km.

impact of OSC on wind field (here we refer to relative wind field) depends on the magnitude and relative direction of the current and wind velocities (Figure 6). For example, OSC and winds are in the opposite direction along north of 15°N at the western BoB (Figure 6a), consistent with the strong VVE (~1 m/day) observed there. Although

upwelling/downwelling along the coasts is determined by wind direction, the intensity of upwelling/downwelling increases, especially when wind and OSC are in the opposite direction. However, significant effect on VVE is not observed when both vectors are aligned in the same direction. It is also clear from the Figures 6a and 3a that

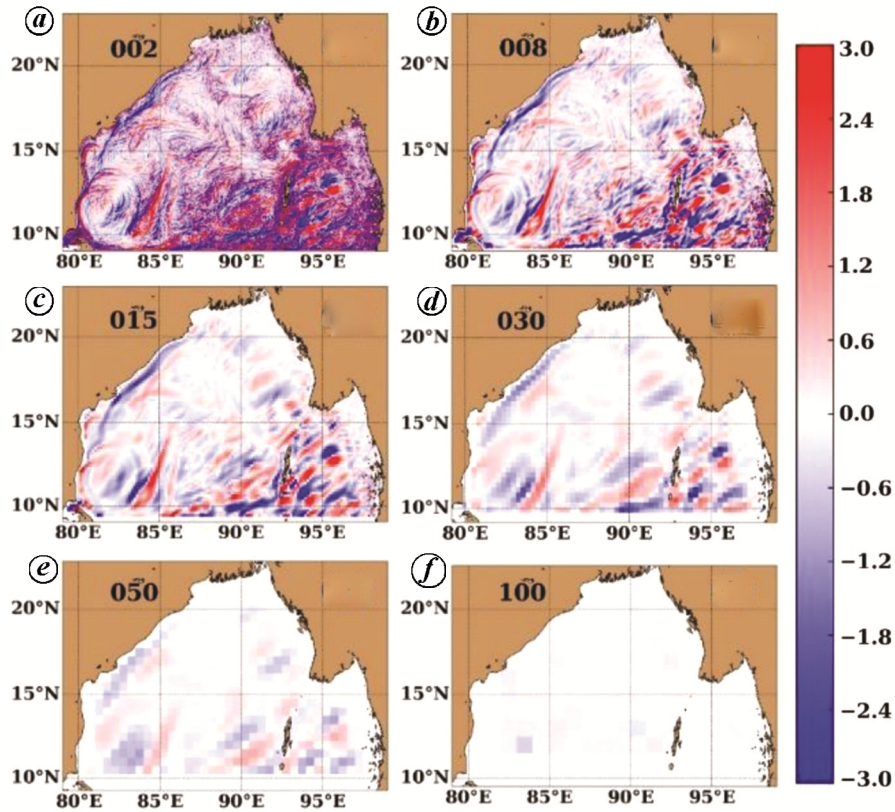


Figure 4. Monthly average of w_z (m/day) for August 2017 for different length scales: (a) 2 km, (b) 8 km, (c) 15 km, (d) 30 km, (e) 50 km and (f) 100 km.

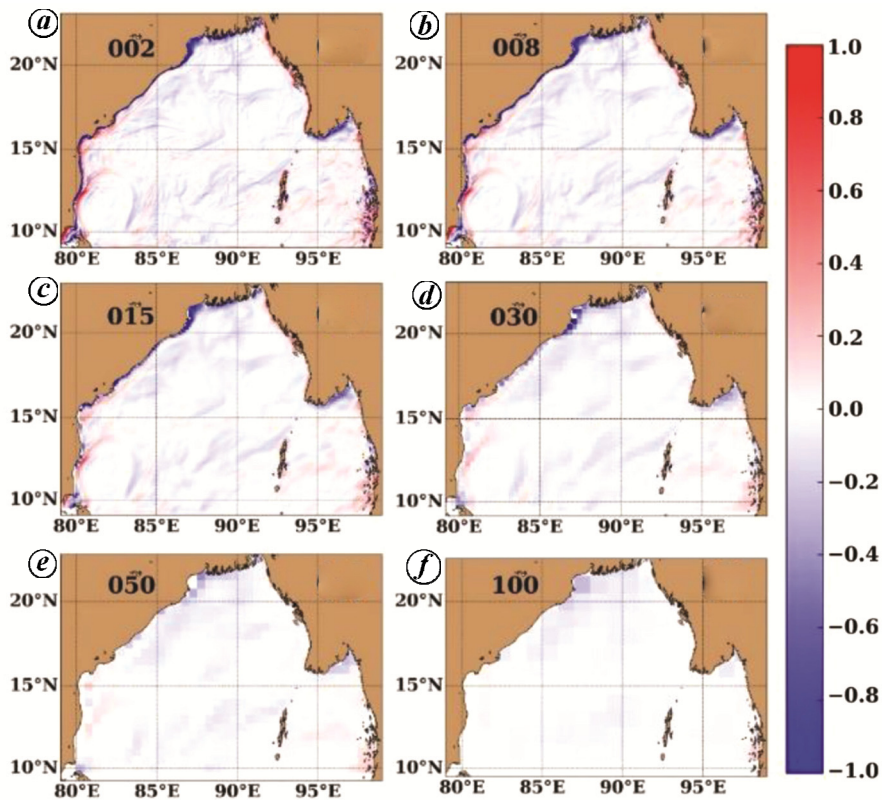


Figure 5. Monthly average of w_{SST} (m/day) for August 2017 for different length scales: (a) 2 km, (b) 8 km, (c) 15 km, (d) 30 km, (e) 50 km and (f) 100 km.

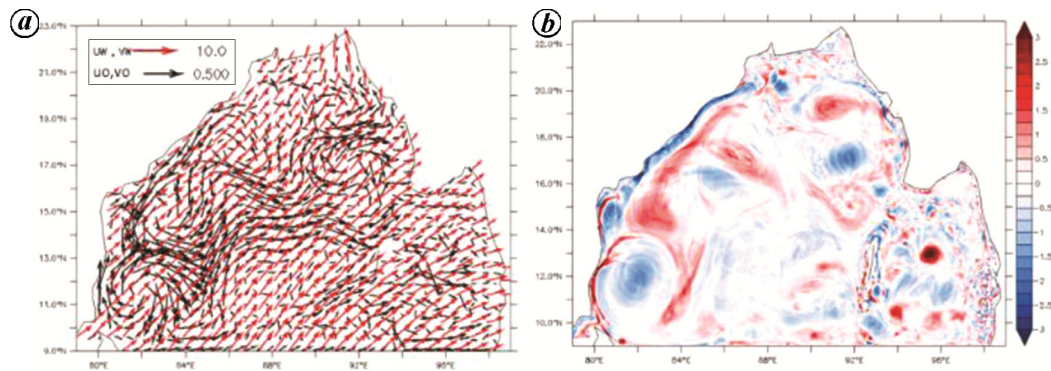


Figure 6. *a*, Vectors of ocean surface current (OSC; u_o and v_o) and wind (u_w and v_w) fields (m/s) for August 2017. *b*, Relative vorticity of OSC (multiplied by $1e5$) for August 2017. Relative vorticity is computed using $\partial v_o/\partial x - \partial u_o/\partial y$.

the relative wind field enhances upwelling/downwelling in cyclonic/anticyclonic mesoscale eddies.

Contribution from surface current vorticity gradient-induced Ekman pumping (w_ζ) is computed and shown in Figure 4 for August 2017. It can be clearly seen from the figure that impact of relative vorticity of OSC is very high for smaller length scales, especially for those less than 10 km. Relative vorticity of OSC introduces dipoles of upwelling and downwelling features, especially over the eddy structures, an observation which is also supported by an earlier study¹⁰. It is mainly due to the enhancement of surface stress over the regions of the eddy, where the absolute wind blows against the rotating eddy surface currents. The southern part of the BoB also shows some predominant features of w_ζ over large length scales (especially <30 km), but are absent almost for 100 km length scale. Monthly average values of w_ζ reach >3 m/day (Figure 4*a*) over the spatial length of 2 km. This large vertical velocity plays a dominant role in the vertical transfer of tracers such as nutrients, temperature, etc. It is observed to be higher along the periphery of mesoscale eddies and the filament structures (fronts associated with eddies) in the ocean (Figures 4*a* and 6*b*). From the spatial structures of the two dominant contributions from OSC to VVE (w_c and w_ζ), it is apparent that the net vertical displacement of water and nutrients is predominantly controlled by w_ζ , especially in the sub-mesoscale range.

SST plays an important role in modifying the low-level winds through the influence of air–sea heat flux on MABL^{18,34}. The differential heating of the lower atmosphere on either side of the SST front decelerates or accelerates the wind as it blows over the SST front⁵. The influence of SST on small-scale variability of VVE is evident from the monthly w_{SST} plot for August 2017 (Figure 5). The influence of SST on VVE is maximum for small scales, and is almost absent for scales larger than 30 km. Sub-mesoscale variability of Ekman pumping is large along the frontal regions of the western boundary of the BoB. This can be attributed to the accelerations and decelerations of surface winds when blowing

across the SST frontal regions, and its effect gets magnified when wind blows parallel to the SST fronts.

After computing SST and OSC-induced VVE for various spatial length scales, variability of VVE is analysed for each case. Strength of the annual variability of VVE for various spatial lengths is analysed using IQR (eq. 8; Figure 7*a*). It can be visible from the figure that VVE is highly energetic at the sub-mesoscale range (2 km) and decreases as the spatial length scale increases. Results support the role played by oceanic spatial length scales in modulating VVE. The unique role of relative vorticity over sub-mesoscale range is clear from Figure 7*a*, as its annual IQR reaches up to 1.14 m/day at 2 km, and decreases sharply towards larger length scales and reaches the value of 0.046 m/day at 100 km. Similarly, the monthly variability of w_{SST} , w_c and w_ζ is also studied using IQR for the spatial length scale mentioned here, and is depicted in Figure 7*b–d* for length scales of 2, 20 and 50 km. It is clear from the figure that VVE exhibits seasonal variability and is consistent over different spatial scales, with a maximum variability for 2 km and minimum variability for 50 km. However, the influence of SST and OSC on VVE is found to be different for various seasons. Impact of OSC on VVE is maximum during monsoon periods (summer and winter monsoons) and minimum during the inter-monsoon period (Figure 7*c* and *d*). Peak value in both w_c and w_ζ is observed during the June–August period and is obvious because currents are strong during summer monsoon. Maximum influence on VVE is observed from the relative vorticity and is almost 11 and five times greater compared to the influence due to SST and relative wind field respectively, at 2 km scale.

To study the relative contributions of SST and OSC on VVE, total Ekman pumping (w_{tot}) is computed as a sum of the current-induced Ekman pumping (w_c and w_ζ) and SST-induced Ekman pumping (w_{SST}). Area-averaged root mean square (RMS) values of w_{tot} , w_{SST} , w_c and w_ζ are computed for the domain of interest (Figure 8). Sharp increase in Ekman pumping velocity is observed from 100 to 2 km length scales due to the influence of SST and

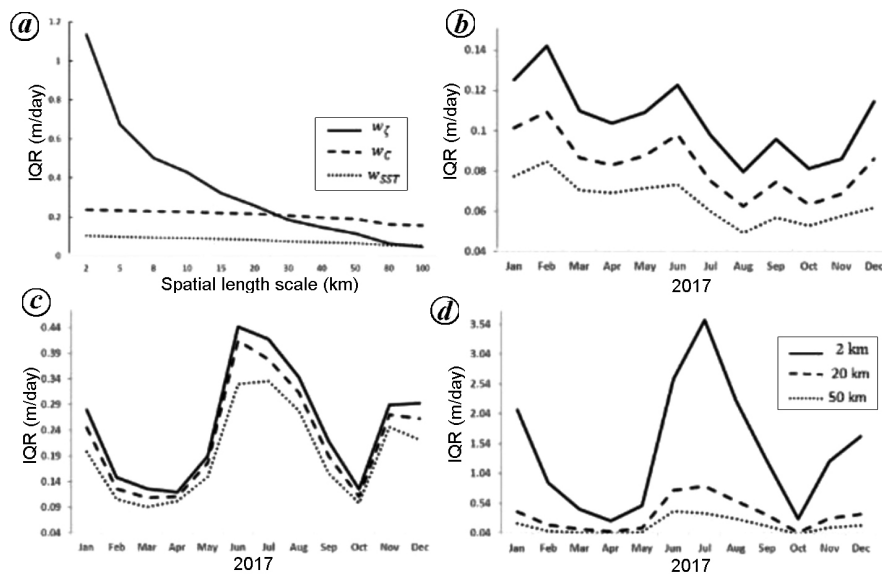


Figure 7. (a) Annual interquartile ranges of w_{SST} , w_c and w_z over various spatial length scales. Time series of interquartile range for (b) w_{SST} , (c) w_c and (d) w_z at spatial scales of 2, 20 and 50 km.

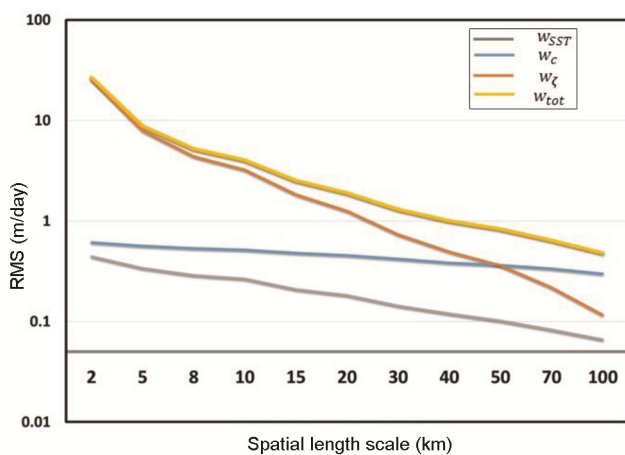


Figure 8. RMS of vertical velocity of Ekman pumping (m/day) over different oceanic length scales (<100 km). Different colours indicate ‘w’ computed differently using equations 4–7.

OSC. However, for length scales less than 10 km, influence of relative vorticity of OSC increases drastically and w_{tot} is predominantly controlled by w_z only. At 2 km length scale, the RMS value of w_z reaches up to 30 m/day, which is highly significant for the vertical transport of tracers such as nutrients into the upper surface layers.

Conclusion

Ocean dynamics influences the vertical velocity of Ekman pumping through air–sea interaction. Here SCATSAT-1 forced OGCM simulations are used to study the ocean dynamics induced Ekman pumping in the BoB. SST and power spectra of simulated SLA at smaller wavelengths using SCATSAT-1 winds match well with the observations compared to simulations forced by NCMRWF winds. Mechanisms involved in understanding

the influence of SST and OSC on wind fields are also studied. The first contribution of OSC to total VVE results from the relative wind that contributes to the intensity of downwelling and upwelling in the BoB, especially along the regions of strong coastal current and mesoscale eddies. The second contribution comes from the vorticity gradient-induced Ekman pumping, which is responsible for the dipole feature of Ekman upwelling and downwelling. Maximum effect on VVE occurs during the Indian summer monsoon, where monthly averaged w_z becomes ~ 3 m/day at 2 km length scale. This magnitude of vertical velocity can modulate the transport of nutrients and other tracers to the surface, and vice versa. w_z is observed to be high along the periphery of mesoscale eddies and along the filament structures. Impact of SST on the computation of VVE is least amongst the three factors and is significant only up to length scales of 30 km; for example, over the SST fronts. It is found that the oceanic spatial scales and seasonality play a major role in the variability of VVE. The influence of OSC on VVE is found to be maximum during the monsoon period and minimum during inter-monsoon period. Maximum influence on VVE is observed from the relative vorticity, which is almost 11 and 5 times greater compared to the influence due to SST and relative wind fields respectively, at 2 km scale. Relative contribution from w_{SST} , w_c and w_z to the total Ekman pumping is also studied by computing RMS of each component for different length scales. A drastic increase of relative vorticity-induced Ekman pumping velocity in the sub-mesoscale is observed, where w_{tot} is predominantly controlled by w_z only. The present study acquires significance in studies pertaining to ocean bio-geochemistry modelling for understanding the role of vertical velocity in tracer transport.

1. Klein, P. and Lapeyre, G., The Oceanic vertical pump induced by mesoscale and submesoscale turbulence. *Annu. Rev. Mar. Sci.*, 2009, **1**, 351–375.
2. Brannigan, L., Intense submesoscale upwelling in anticyclonic eddies. *Geophys. Res. Lett.*, 2016, **43**, 3360–3369; doi:10.1002/2016GL067926.
3. Pickett, M. H. and Paduan, J. D., Ekman transport and pumping in the California current based on the US Navy's high resolution atmospheric model (COAMPS). *J. Geophys. Res.*, 2003, **108**(C10), 3327; doi:10.1029/2003JC001902.
4. Thushara, V. and Vinayachandran, P. N., Formation of summer phytoplankton bloom in the northwestern Bay of Bengal in a coupled physical–ecosystem model. *J. Geophys. Res. Oceans*, 2016, **121**, 8535–8550; doi:10.1002/2016JC011987.
5. Chelton, D. B., Schlax, M. G., Freilich, M. H. and Milliff, R. F., Satellite measurements reveal persistent small-scale features in ocean winds. *Science*, 2004, **303**, 978–983.
6. Sharma, R., Agarwal, N., Chakraborty, A., Mallick, S., Buckley, J., Shesu V. and Tandon, A., Large-scale air–sea coupling processes in the Bay of Bengal using space-borne observations. *Oceanography*, 2016, **29**(2), 192–201; <http://dx.doi.org/10.5670/oceanog.2016.51>.
7. Jensen, T. G. *et al.*, Submesoscale features and their interaction with fronts and internal tides in a high-resolution coupled atmosphere–ocean–wave model of the Bay of Bengal. *Ocean Dyn.*, 2018, **68**, 391; <https://doi.org/10.1007/s10236-018-1136-x>.
8. Wijesekera, H. W. *et al.*, ASIRI: an ocean–atmosphere initiative for Bay of Bengal. *Bull. Am. Meteorol. Soc.*, 2016, **97**, 1859–1884; <https://doi.org/10.1175/BAMS-D-14-00197.1>.
9. Chelton, D. B. and Xie, S., Coupled ocean–atmosphere interaction at oceanic mesoscales. *Oceanography*, 2010, **23**, 52–69; doi:10.5670/oceanog.2010.05.
10. Gaube, P., Chelton, D. B., Samelson, R. M., Schlax, M. G. and O'Neill, L. W., Satellite observations of mesoscale eddy induced Ekman pumping. *J. Phys. Oceanogr.*, 2016, **45**(104), 131; doi:10.1175/JPO-D-14-0032.1.
11. McGillicuddy Jr, D. J., Mechanisms of physical–biological–biogeochemical interaction at oceanic mesoscale. *Annu. Rev. Mar. Sci.*, 2016, **8**, 125–159.
12. Ledwell, J. R., Watson, A. J. and Law, C. S., Evidence for slow mixing across the pycnocline from an open-ocean tracer-release experiment. *Nature*, 1993, **364**, 701–703.
13. McWilliams, J. C., Submesoscale currents in the ocean. *Proc. R. Soc. A: Math. Phys. Eng. Sci.*, 2016, **472**(2189), 20160117; <http://dx.doi.org/10.1098/rspa.2016.0117>.
14. Mahadevan, A. and Tandon, A., An analysis of mechanisms for submesoscale vertical motion at ocean fronts. *Ocean Model.*, 2006, **14**, 241–256.
15. Wei, Y., Zhang, R.-H. and Wang, H., Mesoscale wind stress–SST coupling in the Kuroshio extension and its effect on the ocean. *J. Oceanogr.*, 2017, **73**(6), 785–758; doi:10.1007/s10872-017-0432-2.
16. O'Neill, L. W., Wind speed and stability effects on coupling between surface wind stress and SST observed from buoys and satellite. *J. Climate*, 2012, **25**, 1544–1569; doi:10.1175/JCLI-D-11-00121.1.
17. Small, R. J. *et al.*, Air–sea interaction over ocean fronts and eddies. *Dyn. Atmos. Oceans*, 2008, **45**, 274–319.
18. Seo, H., Miller, A. J. and Roads, J. O., The Scripps coupled Ocean–Atmosphere Regional (SCOAR) model, with applications in the eastern Pacific sector. *J. Clim.*, 2007, **20**, 381–402.
19. Okumura, Y., Xie, S.-P., Numaguti, A. and Tanimoto, Y., Tropical Atlantic air–sea interaction and its influence on the NAO. *Geophys. Res. Lett.*, 2001, **28**, 1507–1510.
20. Agarwal, N., Sharma, R., Basu, S. K., Sarkar, A. and Agarwal, V. K., Evaluation of relative performance of QuikSCAT and NCEP re-analysis winds through simulations by an OGCM. *Deep Sea Res. Part I: Oceanogr. Res. Pap.*, 2007, **54**(8), 1311–1328.
21. Deb, S. K., Bhowmick, S. A., Kumar, R. and Sarkar, A., Inter-comparison of numerical model generated surface winds with QuikSCAT winds over the Indian Ocean. *Mar. Geodesy*, 2009, **32**(4), 391–408.
22. Jaeger, G. S. and Mahadevan, A., Submesoscale selective compensation of fronts in a salinity-stratified ocean. *Sci. Adv.*, 2018, **4**(2); doi:10.1126/sciadv.1701504.
23. Adcroft, A., Hill, C., Campin, J. M., Marshall, J. and Heimbach, P., Overview of the formulation and numerics of the MIT GCM. In Proceedings of the ECMWF Seminar Series on Numerical Methods, 2004, pp. 139–149.
24. Sindhu, B., Suresh, I., Unnikrishnan, A. S., Bhatkar, N. V., Neetu, S. and Michael, G. S., Improved bathymetric datasets for the shallow water regions in the Indian Ocean. *J. Earth Syst. Sci.*, 2007, **116**(3), 261–274.
25. Mallick, S. K., Agarwal, N., Sharma, R. and Prasad, K. V. S. R., Sensitivity of upper ocean dynamics in high-resolution tropical Indian Ocean model to different flux parameterization: case study for the Bay of Bengal (BoB). *Int. Arch. Photogramm. Remote Sensing Spatial Inf. Sci.*, 2018, 839–847; <https://doi.org/10.5194/isprs-archives-XLII-5-839-20>.
26. Dee, D. *et al.*, The era-interim reanalysis: configuration and performance of the data assimilation system. *Q. J. Roy. Meteorol. Soc.*, 2011, **137**, 553–597; doi:10.1002/qj.828.
27. Papa, F., Durand, F., Rossow, W. B., Rahman, A. and Bala, S. K., Satellite altimeter-derived monthly discharge of the Ganga–Brahmaputra River and its seasonal to interannual variations from 1993 to 2008. *J. Geophys. Res.: Oceans*, 2010, **115**(C12); <https://doi.org/10.1029/2009/C006075>.
28. Yaremchuk, M., Yu, Z. and McCreary, J., River discharge into the Bay of Bengal in an inverse ocean model. *Geophys. Res. Lett.*, 2005, **32**(16); <https://doi.org/10.1029/2005GL023750>.
29. Mandal, S., Sil, S., Shee, A., Swain, D. and Pandey, P. C., Comparative analysis of SCATSAT-1 gridded winds with buoys, ASCAT and ECMWF winds in the Bay of Bengal. *IEEE J. Selected Top. Appl. Earth Observ. Remote Sensing*, 2018, **11**(3), 845–851; doi:10.1109/JSTARS.2018.2798621.
30. Stern, M., Interaction of a uniform wind stress with a geostrophic vortex. *Deep-Sea Res. Oceanogr. Abstr.*, 1965, **12**, 355–367; doi:10.1016/0011-7471(65)90007-0.
31. Chelton, D., Schlax, M. G. and Samelson, R. M., Summertime coupling between sea surface temperature and wind stress in the California current system. *J. Phys. Oceanogr.*, 2007, 495–517.
32. Wortham, C. and Wunsch, C., A multidimensional spectral description of ocean variability. *J. Phys. Oceanogr.*, 2014, **44**, 944–966; doi:10.1175/JPO-D-13-0113.1.
33. Biri, S., Serra, N., Scharffenberg, M. G. and Stammer, D., Atlantic sea surface height and velocity spectra inferred from satellite altimetry and a hierarchy of numerical simulations. *J. Geophys. Res.*, 2016, **121**, 4157–4177; doi:10.1002/2015JC011503.
34. Seo, H., Murtugudde, R., Jochum, M. and Miller, A. J., Modeling of mesoscale coupled ocean–atmosphere interaction and its feedback to ocean in the western Arabian Sea. *Ocean Model.*, 2008, **25**, 120–131.

ACKNOWLEDGEMENTS. We thank the Director, Space Applications Centre (SAC; ISRO), Ahmedabad for motivation and we also thank the Deputy Director, Earth, Ocean, Atmosphere, Planetary Sciences and Applications Area and the Group Director, Atmospheric and Oceanic Sciences Group, SAC, for encouragement. Computing facility provided by the MOSDAC team, SAC-ISRO, Ahmedabad is also acknowledged.

doi: 10.18520/cs/v117/i6/993-1001